

# Path Planning Methodology for Multi-Layer Welding of Intersecting Pipes Considering Collision Avoidance

M. Shahabi<sup>†</sup>, H. Ghariblu<sup>†\*</sup> , M. Beschi<sup>‡</sup> and N. Pedrocchi<sup>‡</sup>

<sup>†</sup> *Mechanical Engineering Department, University of Zanjan, Zanjan, Iran*

<sup>‡</sup> *Institute of Intelligent Industrial Technologies and Systems for Advanced Manufacturing - National Research Council, Milan, Italy*

(Accepted August 12, 2020)

## SUMMARY

The V-groove joint of thick wall intersecting pipes must be filled by multi-layer weld. The welding path of intersecting pipes is complicated, and hence multi-layer welds increase the complexity of the problem. This paper proposes a methodology for path planning of multi-layer weld of thick wall intersecting pipes. The methodology is based on measuring the electrode pose located in both side and front views of intersecting pipes. In order to compensate for the path deviation around the pipe circumference, the measured values are used to interpolate the path of each pass between two views. The methodology has been applied in a case study. Simulation results approve that multi-layer weld appropriately fills the V-groove joint space around the pipe circumference. In addition, collision avoidance between welding torch and pipes is considered by introducing a safety ring. While the robot wrist moves inside the safety ring, no collision occurs. Simulation results show the robustness of the proposed path planning method, introduced for collision avoidance.

**KEYWORDS:** Path planning; Multi-layer welding intersecting pipes; Obstacle avoidance.

## 1. Introduction

Multi-layer welding is widely used in the fabrication of pressure vessels, ship structures, and other products that have thick plates or walls. The advantages of automatic welding in comparison to manual or semi-automatic welding are to save the operation time, increase the weld quality and persuade the industry owners to use automatic and robotic welding. The initial setting of robotic welding needs a teaching process and an appropriate setting for welding parameters. Some researchers have tried to reduce the setting and teaching time of multi-layer welding. For example, Moon et al.<sup>1</sup> proposed a method to predict the optimal welding parameters that simplified the teaching process and reduced the requirements of parameters of each layer and each pass in multi-layer welding. Kim et al.<sup>2</sup> developed an automatic welding system for multi-layer and multi-pass welding. They used submerged arc welding for welding of ship structures. Wu et al.<sup>3</sup> proposed a methodology for automated bead layout for robotic multi-pass welding. They considered the size of the ideal welded bead to be constant, and further determined the electrode angle at different passes.

Another concern in the multi-layer robotic welding is the geometry deviations from the nominal state. To overcome this issue, some researchers used vision sensors. For example, Yang et al.<sup>4</sup> proposed a method for multi-pass path planning for a thick plate based on using the information related to two sensors installed on two welding robots simultaneously in order to correct the path, based on

\* Corresponding author. E-mail: [ghariblu@znu.ac.ir](mailto:ghariblu@znu.ac.ir)

the groove size and assembly gap changes. He et al.<sup>5</sup> detected the weld seam profile and extracted the feature points for multi-pass route planning based on the visual attention model. Gu et al.<sup>6</sup> investigated the autonomous seam acquisition and tracking system for multi-pass welding based on the vision sensor. Liu et al.<sup>7</sup> proposed an approach to the path planning of intersecting pipes weld seam on non-ideal models.

Thermal stress, due to high-input heating in multi-layer welding, is another concern. Factors like optimizing the welding sequence, the position of the fixing clamps, the structural geometry, and the welding parameters in robotic multi-layer welding can overcome this issue. For example, Xinghui et al.<sup>8</sup> analysed the welding stress in multi-pass welding on large welded structures and optimized the above factors in robotic welding.

Besides the above-mentioned technical concerns, some researchers have focused on the robot path planning in applications including multi-layer welding. For example, Zhang et al.<sup>9,10</sup> investigated the robot path planning in multi-pass weaving welding for thick plates. Their algorithm found the welding parameters of each pass, the number of layers and passes, and the welding sequence. Ahmed et al.<sup>9</sup> proposed a method for collision-free path planning for multi-pass robotic welding, while the workpiece positioning fixture was considered as an obstacle. Evensen<sup>11</sup> did a comprehensive study on robotic multiple-pass welding of V-groove butt joints. He presented an algorithm that determined the position and orientation of the welding electrode, the weaving amplitude, and the number of passes of each layer based on various parameters such as welding speed, welding wire speed, maximum weaving amplitude and the weld throat.

The above-mentioned literature pivoted around the thick plates multi-layer welding. In other words, the focus was on weld parameters of multi-layer welding. Some other researchers have investigated the robot path planning with complex weld geometry. For instance, Ghariblu and Shahabi<sup>12,13</sup> presented a method for path planning of complex pipe joints with redundant robotic systems. Xianxi et al.<sup>14</sup> also presented an optimal path tracking formulation focusing on the least time and energy consumption for industrial robots. Feng et al.<sup>15</sup> in a study, presented an optimal robot path planning for welding of intersecting pipes. Lu et al.<sup>16</sup> controlled the automated welding on a saddle curve. Chen et al.<sup>17</sup> proposed a method for weld seam path planning of nozzles installed on the spherical head of pressure vessels. Liu et al.<sup>18</sup> presented path planning for the end-effector of the robot in the welding of intersecting pipes. Ren et al.<sup>19</sup> modelled the weld seam and welding torch pose in welding intersected T-shaped pipes. Shi et al.<sup>20,21</sup> proposed an algorithm for industrial robots to weld intersecting pipes. Li et al.<sup>22</sup> used the Solidworks API CAD software for path planning. Liu et al.<sup>23</sup> presented a method for weld seam fitting and welding torch trajectory planning based on non-uniform rational basis spline (NURBS) in intersecting curve welding.

Collision avoidance during robot path planning is another issue. Therefore, path planning of robot manipulators<sup>24–30</sup> and industrial robots<sup>31–34</sup> facing obstacles in different environments have always been an important research topic. The algorithm shall not only avoid the collision but also find the solution in an acceptable time. Researchers proposed different algorithms for collision avoidance.

So far, the robot path planning of multi-layer welding for joints with complicated geometry has not been reviewed in the literature. This is a common application in the cross-pipes welding because of the complex three-dimensional shape of the V-groove joint path. The geometry of V-groove joint changes along the path; as a result, the position of each pass, contrary to the thick plates, is not determined by a simple offset and must be fully specified prior to the operation. This paper addresses the multi-layer welding of intersecting pipes and proposes a methodology based on interpolation to generate the path of multi-layer welds automatically, in addition to obstacle avoidance between the welding torch and intersecting pipes.

Section 2 defines the multi-passes in the multi-layer weld, and determines the position and orientation of each pass with respect to the root pass. Section 3 determines the position and orientation of the root pass in the intersecting pipes. Section 4 illustrates the methodology for path planning of multi-layer weld of intersecting thick pipes. The results of the implanting methodology in a case study are presented in Section 5. In Section 6, a method to involve collision avoidance between welding torch and pipes is presented. In this section, the trajectory involving collision avoidance is planned. Finally, Section 7 discusses the possible research conclusions.

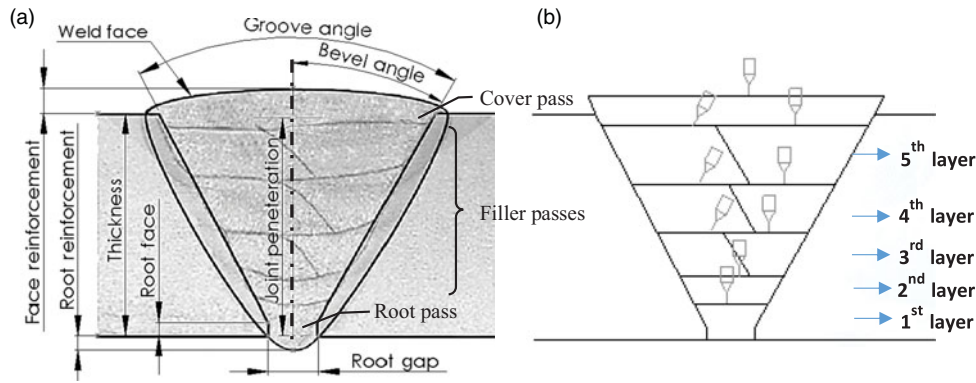


Fig. 1. (a) Multi-layer V-groove weld, (b) simplified state of a weld joint with welding torch orientation.

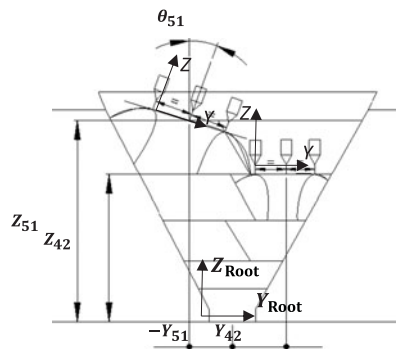


Fig. 2. Weld electrode movement in multi-layer welds.

## 2. Determining Each Pass with Respect to the Root Pass

In multi-layer welding, to create wider a weld width, it is common to weave from side to side along a pass. There are some well-known weaving patterns, weaving frequency, and pitch. The V-groove weld is a common joint in thick-walled welding. Figure 1(a) is a metallography picture that shows the V-groove joint characteristics including nine passes at six layers. The first pass, called root pass, is very important in welding. The correct selection of the root gap and root face guarantees full penetration. The weld size, which is equal to joint penetration, indicates the weld strength. The filler passes fill the joint penetration. Finally, one or more cover passes create a convex weld Face.

Bevel angle, which is half of the groove angle in the symmetric grooves, is selected so that the welding torch can manoeuvre along groove. For example, the bevel angle in GTAW (Gas Tungsten Arc Welding) has to be chosen larger than what is selected for GMAW (Gas Metal Arc Welding) since the size of the welding torch in GTAW is bigger than the torch size of GMAW. Figure 1(b) shows the simplified state of Fig. 1(a). Although here each pass is either diamond (3, 5, and 7 passes) or Trapezium (1, 2, 4, 6, 8, and 9 passes), their geometry will change during intersecting pipe welding. The torch orientation for GMAW welding of each pass is shown in Fig. 1(b), too. Figure 2 shows the weld electrode movement with weaving motion for welding the diamond passes and trapezium passes.

In order to assign coordinate axes to each pass, consider X-axis in the direction of the welding and Z-axis, which indicates the weld electrode orientation (Fig. 2). The right-hand law determines the Y-axis. The terms  $Z_{ab}$ ,  $Y_{ab}$ ,  $\theta_{ab}$  indicate the amount of Z, Y,  $\theta$  of b-pass in a-layer, respectively. Now, each pass can be stated in the root pass coordinate system (CS) using a homogenous matrix,  ${}^{Root}T_{Pass_i}$ .

$${}^{Root}T_{Pass_i} = Tran_{z,Z_{ab}} \times Tran_{y,Y_{ab}} \times Rot_{X,\theta_{ab}} \quad (1)$$

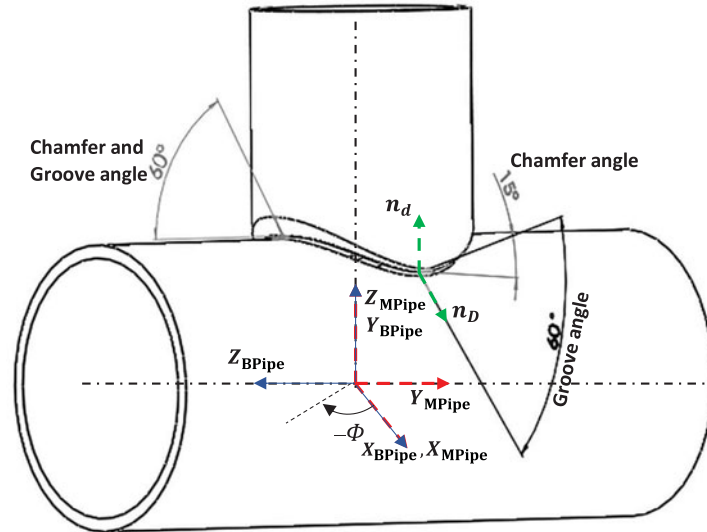


Fig. 3. Variable chamfer angle in the branch pipe results constant 60° groove angle.

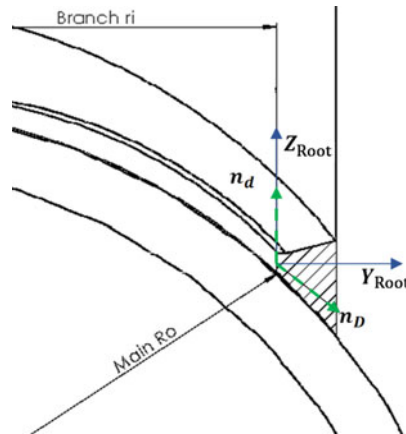


Fig. 4. Root CS assignment.

### 3. Root Pass in Intersecting Pipes

In the previous section, the pass CS with respect to the root was presented. Here, the root CS is defined with respect to the MPipe CS, which is located in the centre of the main pipe. In the thick-walled pipes joint welding, a chamfer on one pipe, either the main pipe or branch pipe is necessary. In this paper, a pipe-to-pipe connection with chamfering on the branch pipe is considered, which is more common in industry (Fig. 3). In this figure, the chamfer angle varies around the pipe circumference from 15° to 60° to keep the groove angle constant at 60°. The origin of MPipe and Bpipe CSs are placed in the intersection of the main pipe and branch pipe axes, while they are depicted by dashed red and solid blue lines, respectively. Also, the welding points are defined as a function of  $\Phi$  in Bpipe CS, and are then mapped to the MPipe CS.

Generally, a 2–4-mm root gap is considered to guarantee full weld penetration. As shown in Fig. 4, the origin of the root CS with subscript “Root” is depicted by blue lines, and is located in the middle of the root gap. Also, unit vectors  $n_d$  and  $n_D$  of the branch and main pipes are depicted by the green dashed lines and placed at the origin of the root CS.

Then the origin of root CS is located on the intersection of two following pipes:

$$\begin{aligned} d &= 2r_i \\ D &\approx 2R_o + \frac{\text{Root gap}}{2} \end{aligned} \quad (2)$$

where  $r_i$  is the branch pipe inner radius,  $R_o$  is the main pipe outer radius. The  $X_{\text{Root}}$  axis, which represents the weld seam moving direction, is perpendicular to the plane made by these two vectors. The  $Z_{\text{Root}}$  coincides with  $n_d$ , and right-hand law determines the  $Y_{\text{Root}}$ . Therefore, Eq. (3) expresses the unit vectors of root CS, while  $n_d$  and  $n_D$  in MPipe CS, whose  $Y$ -axis coincides with the main pipe axis and its  $X$ -axis and  $Z$ -axis are perpendicular to the  $Y$ -axis, comes from Eq. (4).<sup>20</sup>

$$\begin{cases} I = \frac{n_d \times n_D}{|n_d \times n_D|} \\ J = \frac{n_d}{|n_d|} \\ K = I \times J \end{cases} \quad (3)$$

Where,

$$\begin{cases} n_d = [\sin \Phi & -\cos \Phi & 0] \\ n_D = \left[ \frac{r_i \sin \Phi}{R_o} & 0 & \frac{\sqrt{R_o^2 - (r_i \sin \Phi)^2}}{R_o} \right] \end{cases} \quad (4)$$

where  $\Phi$ , as shown in Fig. 3, represents the position of root CS origin and varies with respect to the BPipe CS. Figure 3 shows the BPipe CS, whose  $Y$ -axis coincides with branch pipe direction and whose  $Z$ -axis coincides with the main pipe direction. Now, the points in the root with respect to the BPipe CS is defined.

$${}^{\text{BPipe}}g(\Phi) = \begin{cases} X_{\text{BPipe}} = r_i \sin \Phi \\ Y_{\text{BPipe}} = \sqrt{R_o^2 - X_{\text{BPipe}}^2} \\ Z_{\text{BPipe}} = r_i \cos \Phi \end{cases} \quad (5)$$

For solving the robot kinematic, the definition of points in the MPipe CS is required. According to the Fig. 3:

$${}^{\text{MPipe}}_{\text{BPipe}}T = \begin{bmatrix} 1 & 0 & 0 & 0 \\ 0 & \cos \pi/2 & -\sin \pi/2 & 0 \\ 0 & \sin \pi/2 & \cos \pi/2 & 0 \\ 0 & 0 & 0 & 1 \end{bmatrix} \quad (6)$$

And, then:

$${}^{\text{MPipe}}g(\theta) = {}^{\text{MPipe}}_{\text{BPipe}}T {}^{\text{BPipe}}g(\theta) = \begin{cases} r_i \sin \Phi \\ -r_i \cos \Phi \\ \sqrt{R_o^2 - (r_i \sin \Phi)^2} \end{cases} \quad (7)$$

Finally, the root path can be expressed in MPipe CS using the homogenous transfer matrix  ${}^{\text{MPipe}}_{\text{Root}}T$ :

$${}^{\text{MPipe}}_{\text{Root}}T = \begin{bmatrix} I & J & K & {}^{\text{MPipe}}g(\Phi) \\ 0 & 0 & 0 & 1 \end{bmatrix} \quad (8)$$

where  $I, J, K$ , and  ${}^{\text{MPipe}}g(\Phi)$  are expressed in Eq. (3) and Eq. (7).

#### 4. Methodology for Path Planning of Multi-layer Weld of Intersecting Pipes

Figure 5 shows the groove joint of the pipes from both side and front views. It also shows the root CS and the pass CS, the second pass of the fourth layer. According to the definition of root CS in Section 3, the root CS is fixed, but cross-section of weld groove as well as origin and orientation of passes CS (and obviously pass 4-2 in Fig. 5 has changed in two views).

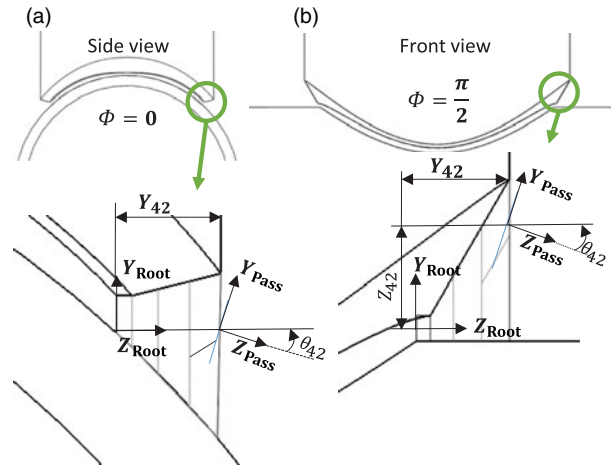


Fig. 5. The position and orientation of the passing frame depend on  $\Phi$ .

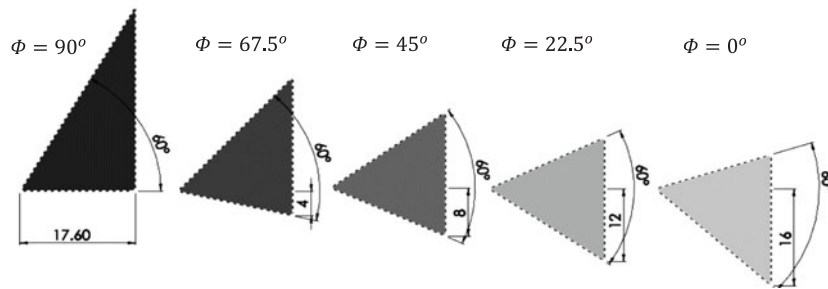


Fig. 6. Cross-sectional area of the weld groove in a quarter of the pipe circumference.

In Fig. 5,  $Y_{42}$  is constant because the weld size and the number of layers around the pipe circumference are constant. In order to compensate for the deviation of the origin position and orientation of the weld pass CS, relative to the root CS, around the pipe circumference, the  $Z_{ab}(\Phi)$ ,  $\theta_{ab}(\Phi)$  variables in Eq. (1) must be defined as a function of  $\Phi$ . This method is based on measuring these values in the side and front views, which are indicated by  $\Phi = 0$ ,  $\Phi = \frac{\pi}{2}$  in the Fig. 5. The interpolation between them in a quadrant of the pipe circumference is calculated. Using interpolation gives flexibility to the control system because its parameters can be controlled during the welding operation.

$$\begin{cases} Z_{ab} = \frac{(Z_{ab1} - Z_{ab0})}{\left(\frac{\pi}{2}\right)}(\Phi) + Z_{ab1} \\ \theta_{ab} = \frac{(\theta_{ab1} - \theta_{ab0})}{\left(\frac{\pi}{2}\right)}(\Phi) + \theta_{ab1} \end{cases} \quad (9)$$

where  $\Phi$  represents the position of the weld groove cross-section in radians,  $Z_{ab1}$ ,  $\theta_{ab1}$  are  $Z_{ab}$ ,  $\theta_{ab}$  at  $\Phi = \frac{\pi}{2}$  as shown in Fig. 5 and  $Z_{ab0}$ ,  $\theta_{ab0}$  are  $Z_{ab}$ ,  $\theta_{ab}$  at  $\Phi = 0$ . As a result, Fig. 6 shows the changes in the cross-sectional area of the weld groove in a quarter of the pipe circumference at five intermediate points  $\Phi = 0^\circ$ ,  $22.5^\circ$ ,  $45^\circ$ ,  $67.5^\circ$ ,  $90^\circ$ . In this figure, the root gap is not considered.

By inserting Eq. (9) into Eq. (1) and considering Eq. (8), the weld seam path around the pipe circumference in each pass relative to the MPipe CS is determined as:

$${}^{\text{MPipe}}_{\text{Poss}_i} T = {}^{\text{MPipe}}_{\text{Root}} T {}^{\text{Root}}_{\text{Poss}_i} T \quad (10)$$

Figure 7 shows the algorithm for generating the Cartesian multi-layer weld path of intersecting pipes. In the following, the application of this algorithm is shown in a case study.

The initial estimation of the multi-layer weld parameters in the second step is obtained from the welding of two plates with similar thicknesses. In the next section, one of these studies has been

Table I. Pipes specifications of the case study.

	Outside diameter (mm)	Thickness (mm)
Main pipe	219	12
Branch pipe	168	10

Table II. Layers characteristics of the Fig. 8, Evensen.<sup>10</sup>

Layer	Pass	$v_1$	$v_2$	$\Delta y$	$\Delta z$	$\Delta \theta$	$W$	Type	Hz
Root	–	90	4.6	0	0	0	1.0	TRIW	1.0
1	1	90	3	0	4.62	0	2.2	TRIW	1.0
2	1	90	3	0	7.27	0	3.7	TRIW	1.0
3	1	90	3	–2.59	11.12	23.1	2.9	ATRAW	1.0
4	2	90	3	3.40	11.12	0	2.5	ATRAW	1.0
Cover	1	90	2	0	12.0	0	7.5	TRIW	1.0

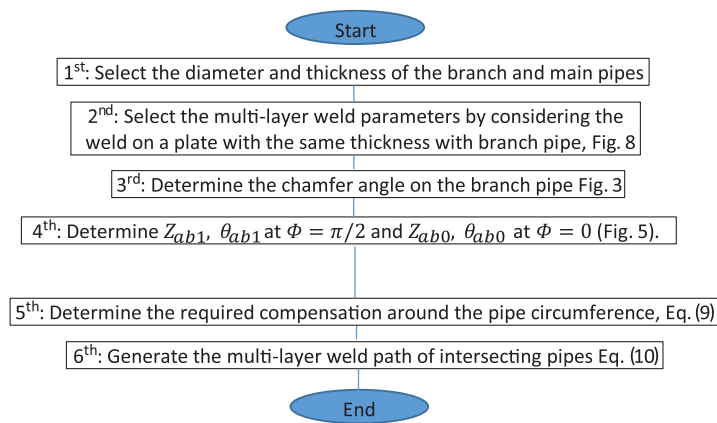


Fig. 7. Algorithm for path planning of multi-layer welds path in intersecting pipes.

reviewed. Figure 6 states the variation of the welding groove around the branch pipe. Since the cross-sectional area of the thick plate welding has been graphed in the next section, Fig. 8 is similar to the welding groove of intersecting pipes at  $\Phi = 22.5^\circ$  (Fig. 6). It would be a good initial estimation for the value of weld parameters in each layer. This initial estimation may be modified slightly by doing practical tests with robotic welding, that is a suggestion for our future work. Meanwhile, due to the small variation of weld groove geometry, as the cross-sectional area of different sections in Fig. 6 shows, the linear interpolation gives an acceptable accuracy.

### 5. Case Study

In this section, the application of this algorithm is explained by means of a case study. In the first step, the main branch pipes geometries are determined. Table I shows the pipe specifications of our case study. It is assumed that main axes of two pipes are perpendicular to each other.

Then, path planning of multi-layer welds of intersecting pipes is computed based on the above-mentioned algorithm. Figure 8 shows the cross-section of a V-groove weld on a thick plate, which has 10 mm thickness. The groove angle is  $60^\circ$ . The weld includes a root layer, three filling layers and a cover layer. The cross-sectional area of the weld groove is similar to the  $\Phi = 22.5^\circ$  (Fig. 6).

Table II shows the layers characteristics of the Fig. 8. Where  $v_1$  is feed speed,  $v_2$  is welding speed,  $W$  and  $Hz$  are respectively weaving amplitude and frequency,  $Type$  indicates the welding process and  $\Delta y, \Delta z, \Delta \theta$  are equal to  $Y_{ab}, Z_{ab}, \theta_{ab}$ , respectively.

In the third step, a suitable chamfer angle is determined regarding the welding process as shown in Fig. 3 for the case study. Then, in the fourth step, the side and front views are drawn as shown in Fig. 5, and  $Z_{ab0}, \theta_{ab0}, Z_{ab1}, \theta_{ab1}, Y_{ab}$  values for each pass are determined. Table III shows these values for the case study.

Table III. Compensation parameters in front and side views, Fig. 5.

Layer	Passport	$Z_{ab0}$	$\theta_{ab0}$	$Z_{ab1}$	$\theta_{ab1}$	$Y_{ab}$
Root	–	0	0	0	0	0
1	1	–1	0	2	0	2.62
2	1	–3	0	5	0	7.27
3	1	–6	0	6	0	11.12
3	2	0	10	11	30	11.12

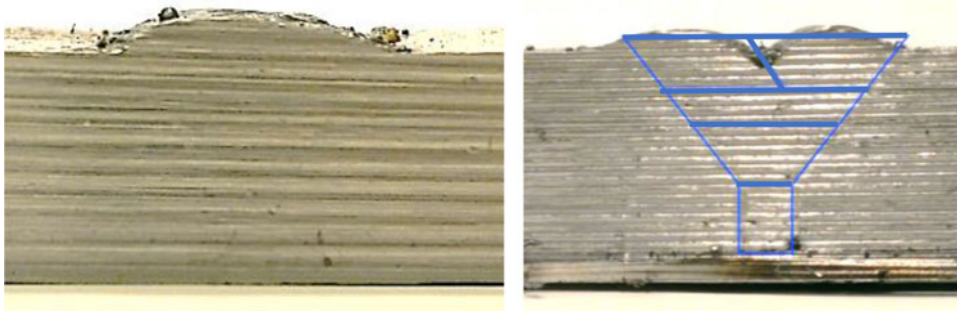


Fig. 8. Multi-layer weld on a sample thick plate with 10-mm thickness, Evensen [10].

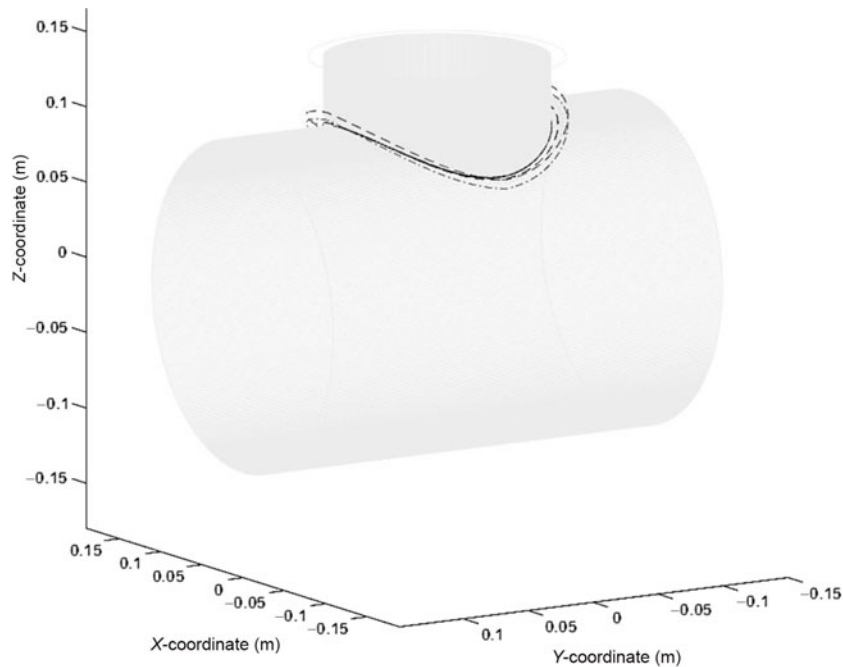


Fig. 9. Multi-layer weld path at the pipe intersection.

By inserting the values of Table III in Eq. (9),  $Z_{ab}(\Phi)$ ,  $\theta_{ab}(\Phi)$  are determined as a function of  $\Phi$ .

Figure 9 shows the weld passes at the intersection of the pipes. In this figure, only the inner wall of the branch pipe is displayed. Meanwhile, Fig. 10 shows the welding passes in the side and front views, where the outer wall of the branch pipe is displayed. The algorithm succeeds to generate the weld path of each pass in the right position.

As an example, Fig. 11 shows how the second pass of the final pass welding (path-32) varies. This figure illustrates the variations in position and orientation of angles with respect to the  $\Phi$  angle around the branch pipe. The orientation angles are actually the first three components of the third column of  ${}^{M_{\text{pipe}}}_{\text{Poss}_i} T$  in Eq. (10).

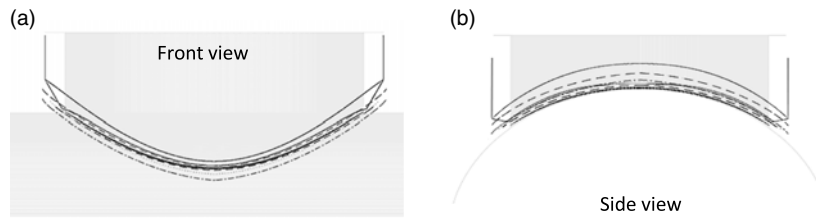


Fig. 10. Welding passes in the side and front views.

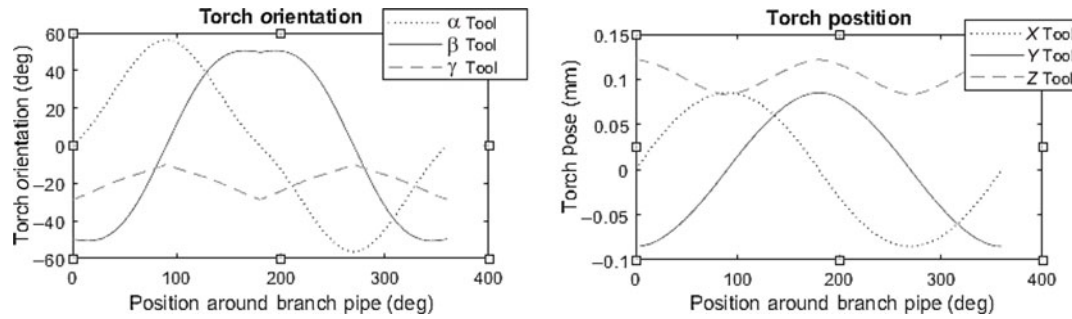


Fig. 11. Variation of the Position and orientation of the final pass.

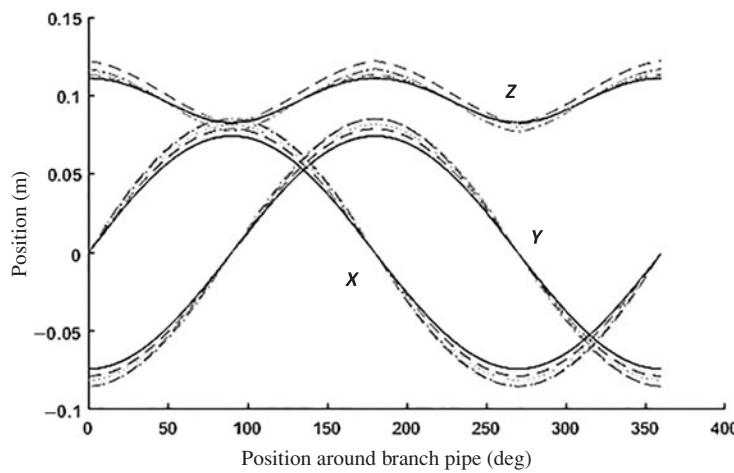


Fig. 12. Changes in path position components in different passes.

Figure 12 illustrates the changes of the position components of the path in different passes. As expected, the changes of  $X$  component at  $\Phi = 0^\circ, 180^\circ$  is zero, while the difference between the various passes is maximum at  $\Phi = 90^\circ, 270^\circ$ . Inversely, the changes of  $Y$  component at  $\Phi = 90^\circ, 270^\circ$  are zero, while the difference between the various passes is maximum at  $\Phi = 0^\circ, 180^\circ$ . The changes of  $Z$  component in the first quarter, that is, between  $\Phi = 0^\circ \sim 90^\circ$ , is proportional to the  $Z_{ab0}, Z_{ab1}$  values of the Table III and is alternately repeated in the next three quarters.

### 6. Trajectory Planning Considering Obstacle Avoidance

In the previous section, the multi-layer weld path of intersecting pipes is generated using Eq. (10) in the Cartesian space. In order to complete the multi-layer welding path planning described above, the risk of electrode torch and arm collision to the pipes should be taken into account. Figure 13 shows how robot is mounted in the roof as gantry to decrease the collision probability, between welding torch and welded pipes. In this section, a trajectory planning methodology for application of intersecting pipes welding is presented considering collision avoidance between the welding torch and intersecting pipes as shown in Fig. 14.



Fig. 13. Robot mounted in the roof as gantry to decrease collision probability.

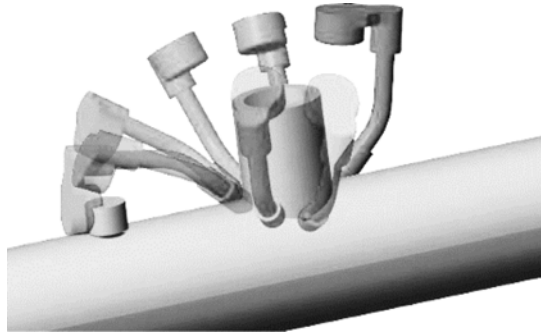


Fig. 14. The probability collision between welding torch and pipes.

In this section, a trajectory planning methodology for application of intersecting pipes welding is presented, considering collision avoidance between the welding torch and intersecting pipes.

### 6.1. Path definition with respect to the robot base

For planning the trajectory, it is required to state the robot movement in its workspace with respect to the robot base. Therefore, Eq. (10) is extended as follows:

$$\mathbf{R}_{Torch}^{\text{Base}} \mathbf{T} = \mathbf{R}_{\text{Fix}}^{\text{Base}} \mathbf{T} \mathbf{M}_{\text{Pipe}}^{\text{Fix}} \mathbf{T} \mathbf{M}_{\text{Root}}^{\text{Pipe}} \mathbf{T} \mathbf{R}_{\text{Poss}_i}^{\text{Root}} \mathbf{T} \mathbf{T}_{\text{Torch}}^{\text{Poss}_i} \mathbf{T} \quad (11)$$

where  $\mathbf{M}_{\text{Pipe}}^{\text{Fix}} \mathbf{T}$  and  $\mathbf{R}_{\text{Fix}}^{\text{Base}} \mathbf{T}$  are homogenous transformation matrix that determines the longitudinal position of the torch with respect to the fix CS, respectively.  $\mathbf{T}_{\text{Torch}}^{\text{Poss}_i}$  adds some welding characteristics to the path before the robot moves along the path (Fig. 10). These characteristics include weaving motion to widen the weld width, the electrode extension to control the melting pool, and the electrode angle relative to the work piece, defined in the welding by work and motion angles.

By changing each of the above-mentioned parameters, the welding torch position changes relative to the work pieces. Based on three rotation  $U$ ,  $V$ , and  $W$  define motion angle, work angle, and functional redundancy angle, respectively. Two transformations  $L$  and  $S$  are electrode extension and waving motion, respectively. Then:

$$\mathbf{T}_{\text{Torch}}^{\text{Pass}_i} = \text{Tran}_{y,S} \times \text{Rot}_{x,U} \times \text{Rot}_{y,V} \times \text{Rot}_{z,W} \times \text{Tran}_{z,L} \quad (12)$$

### 6.2. Inverse kinematic solution

The rotation of the end effector around its rotational axis in some applications like welding, cutting, and some others is not important. So, the arc welding is a five DOF task; therefore, conducting arc welding with an industrial six DOF robot results in a kinematic redundancy, called functional

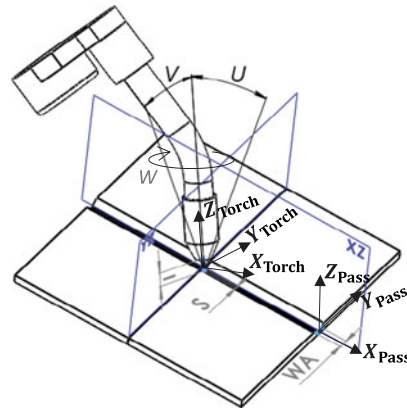


Fig. 15. Multi-path welding parameters.

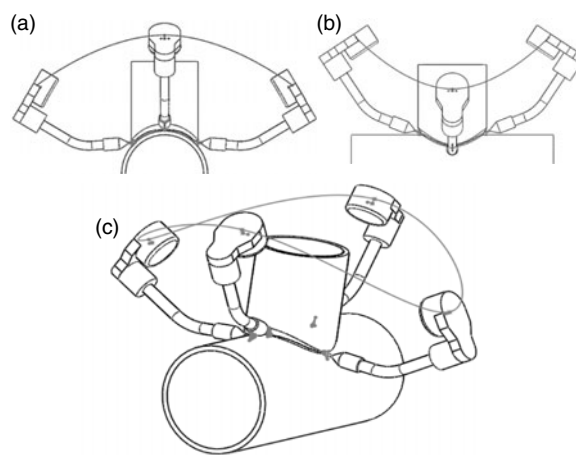


Fig. 16. No collision by selecting w angle. (a) Side view (b) Front view (c) B-Spline curve.

redundancy. This functional redundancy is used in an inverse kinematic solution in order to search within null space, and find the optimal solution. To resolve the functional redundancy, Jacobian based method [35] is used here:

$$\dot{q} = J^{\#} \dot{X} \tag{13}$$

where,  $\dot{X}_{5 \times 1}$  includes the linear and angular velocity of the torch head in the Cartesian space.  $\dot{q}$  is a  $6 \times 1$  vector, including joints speeds, term  $J^{\#}$  is pseudo-inverse of Jacobian and is a  $6 \times 5$  matrix. It is defined as  $J^{\#} = J^T (J J^T)^{-1}$ , where term  $J$  is the Jacobin matrix of order  $5 \times 6$ .

### 6.3. Collision avoidance

One solution to collision avoidance is realized by adding a kinematic constraint in the Cartesian space. In Fig. 16, the welding torch position at the second layer of our multi-layer weld case study is drawn at  $\Phi = 0^\circ, 90^\circ, 270^\circ, 360^\circ$ . The  $w$  angle (Fig. 15) has a constraint value in this case, so the robot wrist stands at the highest position with respect to the top surface of the main pipe. Figure 16(c) shows the B-spline curve of the robot wrist, which is drawn using four mentioned points.

Although it seems that the collision is avoided in Fig. 16, it is not so useful. The reason is that if the robot tends to move exactly along the B-spline path, the end effector cannot follow the path, defined by Eq. (11). This is because B-spline is an approximate solution while Eq. (11) is an exact solution. Instead, to solve this problem, by employing the functional redundancy, the robot wrist is not constrained to move along the B-spline curve, but it is allowed to move inside a volumetric ring named as safety ring (Fig. 17). The main features of the safety ring concept are presented in ref. [32].

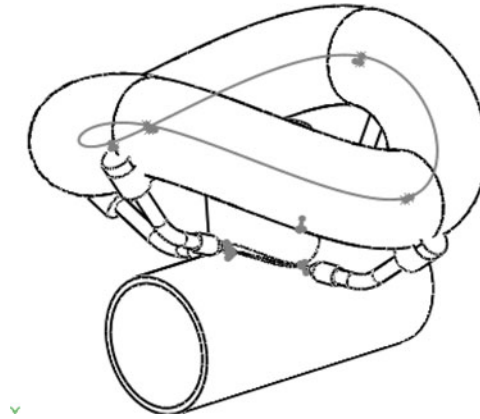


Fig. 17. Generated ring using the B-spline curve of Fig. 16(c).

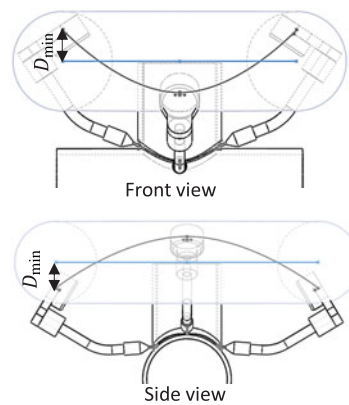


Fig. 18. Using ellipse (blue line) instead of B-spline to create safety ring.

The search into the null space to find the solution is done by adding a projection matrix to Eq. (13)

$$\dot{q} = J^\# \dot{X} + (I_n - J^\# J) \dot{q}_p \quad (14)$$

where  $(I_n - J^\# J)$  is called the projection matrix, which projects the velocities  $\dot{q}_p$  into the null space of Jacobian.  $I_n$  is a  $6 \times 6$  identity matrix.

To simplify the problem, an ellipse instead of B-spline is used, which is difficult to formulate. Figure 18 shows the safety ring, generated by this ellipse. Eq. (13) tries to find  $\dot{q}_p$  that minimized  $D_{\min}$ .

$$\dot{q}_0 = \frac{\partial D_{\min}}{\partial q} \quad (15)$$

where  $D_{\min}$  is the minimum distance between the robot wrist position and safety ring centre line.

$$D_{\min} = \min \|p_{\text{wrist}} - p_{\text{ring centre}}\|_{\phi=0-2\pi} \quad (16)$$

Therefore, by defining the safety ring, the robot wrist moves with no collision with the pipes during the welding operation. On the other hand, collision avoidance needs a lot of computation and inherently involves high-computational cost. The reason is that the focus is on the wrist position, not the wrist orientation, meaning that the computational cost of the proposed method is relatively low.

#### 6.4. Planned trajectory

In this section, the results of implementing a safety ring to avoid the collision for welding layer 3 of our multi-layer weld case study are discussed. Figure 19 shows the robot wrist path, which is inside the safety ring and guarantees no collision.

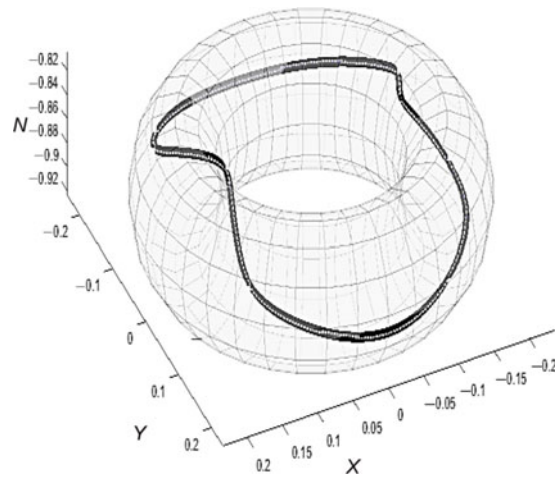


Fig. 19. Robot wrist path.

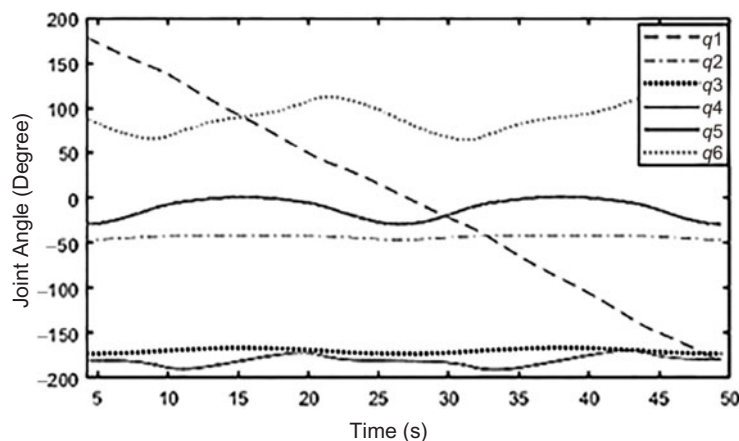


Fig. 20. Joint angle and velocities of the planned trajectory.

Figure 20 shows the history of joint angles of planned trajectory versus time.

## 7. Conclusion

This paper proposes a methodology for path planning for welding multi-layer thick-walled intersecting pipes. This methodology is based on measuring the position and orientation values of electrode pose in side and front views of intersecting pipes. These values were employed to interpolate the path of each pass between two views. Furthermore, to avoid collision between welding torch and welded pipes, the safety ring method was presented in the last section. Simulation results show that the proposed methodology could effectively plan the path of all passes of multi-layer weld without any collision. The simulation also shows that multi-layer weld fills the V-groove joint space around the pipe circumference very well. In this paper, the initial estimation of weld parameters was extracted from experiments, performed in the thick plates welding that may change slightly by doing a practical test on pipe welding joints. This experiment has some implications for our future works.

## References

1. H.-S. Moon and S.-J. Na, "Neuro-Fuzzy System for Predicting Optimal Weld Parameters of Horizontal Fillet Welds," *Proceedings of Asian Pacific Welding Congress* (1996).
2. Y. B. Kim, J. G. Kim, W. T. Jang, J. R. Park, H. S. Moon and J. O. Kim, "Development of automatic welding system for multi-layer and multi-pass welding," *IFAC Proc.* **41**(2), 4290–4291 (2008).
3. Y. Wu, J. Z. M. Go, S. M. Ahmed, W. Lu, C. Chew and C. K. Pang, "Automated Bead Layout Methodology for Robotic Multi-Pass Welding," *In: 2015 IEEE 20th Conference on Emerging Technologies & Factory Automation (ETFA)* (IEEE, Luxembourg, 2015) pp. 1–4.

4. C. Yang, Z. Ye, Y. Chen, J. Zhong and S. Chen, "Multi-pass path planning for thick plate by DSAW based on vision sensor," *Sens. Rev.* **34**(4), 416–423 (2014).
5. Y. He, Y. Xu, Y. Chen, H. Chen and S. Chen, "Weld seam profile detection and feature point extraction for multi-pass route planning based on visual attention model," *Robot. Comput. Integr. Manuf.* **37**, 251–261 (2016).
6. W. Gu, Z. Xiong and W. Wan, "Autonomous seam acquisition and tracking system for multi-pass welding based on vision sensor," *Int. J. Adv. Manuf. Tech.* **69**(1–4), 451–460 (2013).
7. Y. Liu, J. Liu and X. Tian, "An approach to the path planning of intersecting pipes weld seam with the welding robot based on non-ideal models," *Robot. Comput. Integr. Manuf.* **55**, 96–108 (2019).
8. S. Xingkui, Y. Xinhua and W. Yuedong, "Modeling and Simulating for Multi-Pass Welding Process of Large Welded Structures," **In: 2010 International Conference on Digital Manufacturing & Automation (IEEE, 2010).**
9. H. Zhang, H. Lu, C. Cai and S. Chen, "Robot Path Planning in Multi-Pass Weaving Welding for Thick Plates," **In: Robotic Welding, Intelligence and Automation (Springer, 2011) pp. 351–359.**
10. S. M. Ahmed, J. Yuan, Y. Wu, C. M. Chew and C. K. Pang, "Collision-Free Path Planning for Multi-Pass Robotic Welding," **In: 2015 IEEE 20th Conference on Emerging Technologies & Factory Automation (ETFA) (IEEE, 2015).**
11. B. E. Evensen, *Robotic Multiple-Pass Welding of V-Groove Butt Joints* (NTNU, 2016).
12. H. Ghariblu and M. Shahabi, "Path planning of complex pipe joints welding with redundant robotic systems," *Robotica* **37**(6), 1020–1032 (2019)
13. M. Shahabi and H. Ghariblu, "Optimal joint motion for complicated welding geometry by a redundant robotic system," *Eng. Optim.* **52**(5), 875–895 (2020)
14. X. Luo, S. Li, S. Liu and G. Liu., "An optimal trajectory planning method for path tracking of industrial robots," *Robotica*, **37**(3), 502–520 (2019)
15. H. Fang, S. Ong and A. Nee, "Robot path planning optimization for welding complex joints," *Int. J. Adv. Manuf. Tech.* **90**(9–12), 3829–3839 (2017).
16. Y. Lü, X. Tian and J. Liang, *Track Control in Automated Welding of Saddle Curve* (2010).
17. C. Chen, S. Hu, D. He and J. Shen, "An approach to the path planning of tube–sphere intersection welds with the robot dedicated to J-groove joints," *Robot. Comput. Integr. Manuf.* **29**(4), 41–48 (2013).
18. L. Y. Z. J. L. Zhenyang and C. Shujun, "Pose planning for the end-effector of robot in the welding of intersecting pipes," *Chin. J. Mech. Eng.-En.* **24**(2), 1.
19. F. Ren, S. Chen, S. Yin and X. Guan, "Modeling on weld position and welding torch pose in welding of intersected pipes," *Trans. China Weld. Ins.* **29**(11), 33–36 (2008).
20. L. Shi and X. Tian, "Automation of main pipe-rotating welding scheme for intersecting pipes," *Int. J. Adv. Manuf. Technol.* **77**(5–8), 955–964 (2015).
21. L. Shi, X. Tian and C. Zhang, "Automatic programming for industrial robot to weld intersecting pipes," *Int. J. Adv. Manuf. Technol.* **81**(9–12), 2099–2107 (2015).
22. J. Li, L. Li, Z. Dong and D. Song, "An automatic posture planning software of arc robot based on solidworks API," *Mod. Appl. Sci.* **3**(7), 121 (2009).
23. Y. Liu, L. Shi and X. Tian, "Weld seam fitting and welding torch trajectory planning based on NURBS in intersecting curve welding," *Int. J. Adv. Manuf. Technol.* **95**(5–8), 2457–2471 (2018).
24. S. F. Saramago and V. S. Junior, "Optimal trajectory planning of robot manipulators in the presence of moving obstacles," *Mech. Mach. Theory* **35**(8), 1079–1094 (2000).
25. J. Agirrebeitia, R. Avilés, I. F. de Bustos and G. Ajuria, "A new APF strategy for path planning in environments with obstacles," *Mech. Mach. Theory* **40**(6), 645–658 (2005).
26. F. Valero, V. Mata and A. Besa, "Trajectory planning in workspaces with obstacles taking into account the dynamic robot behaviour," *Mech. Mach. Theory* **41**(5), 525–536 (2006).
27. R. Saravanan, S. Ramabalan and C. Balamurugan, "Evolutionary multi-criteria trajectory modeling of industrial robots in the presence of obstacles," *Eng. Appl. Artif. Intell.* **22**(2), 329–342 (2009).
28. R. Menasri, A. Nakib, B. Daachi, H. Oulhadj and P. Siarry, "A trajectory planning of redundant manipulators based on bilevel optimization," *Appl. Math. Comput.* **250**, 934–947 (2015).
29. L. Xiao and Y. Zhang, "Dynamic design, numerical solution and effective verification of acceleration-level obstacle-avoidance scheme for robot manipulators," *Int. J. Syst. Sci.* **47**(4), 932–945 (2016).
30. C. Chen, "Path planning in distorted configuration space," *Robotica* **35**(7), 1585–1597 (2017).
31. F. J. Abu-Dakka, F. Rubio, F. Valero and V. Mata, "Evolutionary indirect approach to solving trajectory planning problem for industrial robots operating in workspaces with obstacles," *Eur. J. Mech.-A/Solids* **42**, 210–218 (2013).
32. F. J. Rubio, et al., "Simultaneous algorithm to solve the trajectory planning problem," *Mech. Mach. Theory* **44**(10), 1910–1922 (2009).
33. F. Rubio, F. Valero, J. L. Sunyer and A. Garrido, "The simultaneous algorithm and the best interpolation function for trajectory planning," *Ind. Robot Int. J.* **37**(5), 441–451 (2010).
34. M. Shahabi, H. Ghariblu and M. Beschi, "Obstacle avoidance of redundant robotic manipulators using safety ring concept," *Int. J. Comput. Integr. Manuf.* **32**(7), 695–704 (2019).
35. F. Fahimi, "Autonomous Robots: Modeling, Path Planning, and Control, vol. 107 (Springer Science & Business Media, 2008).